The Journal of Navigation (2022), **75**:4 832–848
doi:10.1017/S0373463322000017

RESEARCH ARTICLE

A novel partial ambiguity resolution based on ambiguity dilution of precision- and convex-hull-based satellite selection for instantaneous multiple global navigation satellite systems positioning

Xin Liu,[1] Shubi Zhang,[1] Qiuzhao Zhang,[1]* Nanshan Zheng,[1] Wenyuan Zhang,[1] and Nan Ding[2]

[1] School of Environment and Spatial Informatics, China University of Mining and Technology, Jiangsu, China.
[2] School of Geography, Geomatics and Planning, Jiangsu Normal University, Jiangsu, China.
*Corresponding author. E-mail: qiuzhaocumt@cumt.edu.cn

Received: 8 December 2020; **Accepted:** 2 January 2022; **First published online:** 8 February 2022

Keywords: fast and high-precision positioning; partial ambiguity resolution; convex hull; ambiguity dilution of precision

Abstract

Although multiple global navigation satellite systems (multi-GNSS) with more visible satellites have a high success rate, they make positioning time-consuming. Partial ambiguity resolution (PAR) can improve the efficiency of multi-GNSS; however, at present PAR cannot simultaneously achieve fast and high-precision positioning with a high success rate. Therefore, PAR based on ambiguity dilution of precision- and convex-hull-based satellite selection is proposed. The experimental results of the proposed PAR, its corresponding satellite selection algorithm, the classical PAR, and the low-cutoff-elevation-angle-based multi-GNSS show that the proposed PAR outperforms the classical PAR, i.e., it achieves fast and high-precision positioning with a success rate of 100·0%. Furthermore, in terms of R-ratio-test-based ambiguity validation, it improves the reliability of carrier-phase-based integrity monitoring of multi-GNSS and the corresponding satellite selection algorithms. In addition, its positioning accuracy is close to that of multi-GNSS and higher than that of the classical PAR, with maximum differences of 0·3 and 2·4 cm, respectively. The proposed single (dual) frequency-based PAR improves single/dual-frequency multi-GNSS efficiency by more than 54·9%/80·4% (42·0%/75·8%) when 14·4 (13·2) out of 24·4 satellites are selected.

1. Introduction

Global navigation satellite system (GNSS)-based instantaneous (single-epoch) and high-precision positioning has wide applications, such as in deformation monitoring, geological disaster monitoring, and unmanned driving (Han and Rizos, 1999; Yi et al., 2013; Liu et al., 2019). The key to these applications lies in fast, reliable, and correct determination of the integer ambiguity vector, which has long been a major challenge. Although single-epoch single satellite system can realise fast positioning, its ambiguity resolution success rate is low and its positioning is unreliable owing to its weak model (Deng et al., 2014). With the development of the global positioning system (GPS), BeiDou navigation satellite system (BDS), and Galileo, multiple GNSS (multi-GNSS)-based single-epoch positioning has become feasible and its success rate can reach up to 100% for short baselines (Teunissen et al., 2014; Odolinski et al., 2015; Odolinski and Teunissen, 2016). As of March 2021, the GPS has 31 operational satellites (GPS.GOV, 2021). Similarly, there are 26 Galileo satellites in orbit; however, only 22 of them are available for service (European GNSS Service Centre, 2021). Further, there are 15 regional and 29 global BDS satellites that provide positioning services (BeiDou Navigation Satellite System, 2021). Multi-GNSS can improve the geometric strength of the GNSS model, the probability of correct ambiguity

estimation, and the reliability of the positioning system (Yang et al., 2011; Li et al., 2015). However, the large number of observed satellites in multi-GNSS makes positioning time-consuming.

Partial ambiguity resolution (PAR) can improve the computational efficiency by fixing a subset of ambiguities rather than a full set, which includes model- and data-driven PAR (Teunissen et al., 1999; Verhagen et al., 2011; Brack and Christoph, 2014; Brack, 2017). Model-driven PAR includes classical PAR (Teunissen et al., 1999), sequential PAR (Liu et al., 2017), iterative PAR (Parkins, 2011), and satellite-selection-based PAR (Mowlam, 2004; Takasu and Yasuda, 2010). However, for the classical PAR, the integer bootstrapping success rate $P_{s,IB}$ of multi-GNSS can reach up to 100%; thus, $P_{s,IB}$ is no longer suitable as a threshold for selecting the ambiguity subset. Meanwhile, the conservative $P_{s,IB}$ sometimes causes the ambiguity vector to be fixed incorrectly and results in a low success rate. Because the sequential PAR resolves all ambiguities by fixing partial ambiguities in batches, it limits the improvement of the computational efficiency, which is not beneficial for multi-GNSS to achieve fast positioning. Furthermore, the unpredictable number of iterations of the iterative PAR may make positioning more time-consuming. The selected ambiguities of the classical, iterative, and satellite-selection-based PAR commonly correspond to high-elevation-angle satellites, which will result in low positioning accuracy. In addition, ambiguity decorrelation is required in the model- and data-driven PAR, and the higher the dimension of ambiguity vector, the more time-consuming is the decorrelation. Hence, for multi-GNSS, how to rapidly select an optimal subset of ambiguities to achieve fast and high-precision positioning with a high success rate is a critical problem.

Ambiguity dilution of precision (ADOP) is a scalar factor for measuring the ambiguity resolution success rate. To address the above-mentioned limitations of the present PAR, a novel PAR based on ADOP- and convex-hull-based satellite selection (ACPAR) is proposed. The feasibility of ADOP as a threshold of PAR to select partial ambiguities by selecting satellites before ambiguity decorrelation is analysed. Then, ambiguity selection strategies based on ADOP- and convex-hull-based satellite selection are proposed to rapidly determine the optimal ambiguity subset. Specifically, ambiguity selection based on convex-hull-based satellite selection is proposed to select the required ambiguities related to the evenly distributed low-elevation-angle satellites. Further, ambiguity selection based on ADOP-based satellite selection is proposed to select the least number of ambiguities corresponding to the high-elevation-angle satellites. The results of single-epoch GPS/BDS/Galileo relative positioning experiments indicate that ACPAR outperforms the classical PAR, i.e., it achieves fast and high-precision positioning with a success rate of 100·0%. Furthermore, its positioning accuracy is close to that of low-cutoff-elevation-angle-based multi-GNSS (L-multi-GNSS) and much higher than that of the classical PAR. Similar to ADOP- and convex-hull-based satellite selection, it can improve the computational efficiency of L-multi-GNSS considerably, which is higher than that of the classical PAR. Moreover, it can improve the R-ratio-test-based reliability of L-multi-GNSS and the corresponding satellite selection.

The remainder of this paper is organised as follows. Section 2 introduces the GNSS ambiguity resolution theory with the R-ratio test. Section 3 describes the ADOP and convex hull theories. Section 4 introduces the ACPAR. Section 5 discusses the positioning performance of ACPAR on the basis of single-epoch positioning experiments. Finally, Section 6 concludes the paper.

2. GNSS ambiguity resolution

2.1. Full and partial ambiguity resolution modes

The double-difference function and stochastic models of observed satellites are given by Equations (1) and (2), respectively (Teunissen et al., 2014):

$$\boldsymbol{E}\begin{bmatrix}\boldsymbol{p}\\ \emptyset\end{bmatrix}=\begin{bmatrix}\boldsymbol{B} & \boldsymbol{0}\\ \boldsymbol{B} & \boldsymbol{B}_{\lambda}\end{bmatrix}\cdot\begin{bmatrix}\boldsymbol{b}\\ \boldsymbol{a}\end{bmatrix} \tag{1}$$

$$\boldsymbol{D}\begin{bmatrix}\boldsymbol{p}\\ \emptyset\end{bmatrix}=\begin{bmatrix}\boldsymbol{Q}_{\boldsymbol{p}} & \boldsymbol{0}\\ \boldsymbol{0} & \boldsymbol{Q}_{\emptyset}\end{bmatrix}=\begin{bmatrix}\sigma_p^2\boldsymbol{Q} & \boldsymbol{0}\\ \boldsymbol{0} & \sigma_{\emptyset}^2\boldsymbol{Q}\end{bmatrix},\boldsymbol{D}^{-1}=\begin{bmatrix}\boldsymbol{P}/\sigma_p^2 & \boldsymbol{0}\\ \boldsymbol{0} & \boldsymbol{P}/\sigma_{\emptyset}^2\end{bmatrix},\boldsymbol{P}=\boldsymbol{Q}^{-1} \tag{2}$$

https://doi.org/10.1017/S0373463322000017 Published online by Cambridge University Press

where $\boldsymbol{E}[\cdot]$ and $\boldsymbol{D}[\cdot]$ denote the expectation and dispersion operators, respectively; $\boldsymbol{b}$ and $\boldsymbol{a}$ represent the baseline and double-difference ambiguity vectors, respectively; $\boldsymbol{B}$ is a coefficient matrix, and $\boldsymbol{B}_\lambda = \lambda \cdot \boldsymbol{I}_{n\times n}$, where λ is the carrier wavelength and n is the ambiguity vector dimension; $\boldsymbol{Q}$ is the covariance matrix of the double-difference observations with the elevation-dependent weighting model; and σ_p and $\sigma_\emptyset$ are the undifferenced code and phase standard deviations, respectively.

Using the standard least-squares method, the float solutions $\hat{\boldsymbol{b}}$ and $\hat{\boldsymbol{a}}$ with variance-covariance matrices $\boldsymbol{Q}_{\hat{b}}$ and $\boldsymbol{Q}_{\hat{a}}$ can be obtained. The least-squares ambiguity decorrelation adjustment (LAMBDA) can be used to obtain the integer solution of the ambiguity vector in the full ambiguity resolution mode (Teunissen, 1995):

$$\check{\mathbf{z}} = \min_{z\in\tilde{\boldsymbol{Z}}} (\hat{z}-z)^{\mathrm{T}} Q_{\hat{z}}^{-1} (\hat{z}-z) \tag{3}$$

where $\hat{z} = \boldsymbol{Z}\hat{\boldsymbol{a}}$, $Q_{\hat{z}} = \boldsymbol{Z}Q_{\hat{a}}\boldsymbol{Z}^{\mathrm{T}}$, $\boldsymbol{Z}$ represents the decorrelation transform matrix, and $\tilde{\boldsymbol{Z}}$ represents the set of integers. If $\boldsymbol{Z}$ is set as $\left[\boldsymbol{Z}_1^{\mathrm{T}}\ \boldsymbol{Z}_2^{\mathrm{T}}\right]^{\mathrm{T}}$, Equation (3) can be expressed as follows (Li et al., 2015):

$$\begin{cases} \check{z}_1 = \min\limits_{z_1\in\tilde{\boldsymbol{Z}}} (\hat{z}_1 - z_1)^{\mathrm{T}} \boldsymbol{Q}_{\hat{z}_1}^{-1} (\hat{z}_1 - z_1) \\ \check{z}_2 = \min\limits_{z_2\in\tilde{\boldsymbol{Z}}} (\hat{z}_{2/1} - z_2)^{\mathrm{T}} \boldsymbol{Q}_{\hat{z}_{2/1}}^{-1} (\hat{z}_{2/1} - z_2) \end{cases} \tag{4}$$

where $\hat{z}_1 = \boldsymbol{Z}_1\hat{\boldsymbol{a}}$, $\hat{z}_{2/1} = \hat{z}_2 - \boldsymbol{Q}_{\hat{z}_2\hat{z}_1}\boldsymbol{Q}_{\hat{z}_1}^{-1}(\hat{z}_1 - z_1)$, $\hat{z}_2 = \boldsymbol{Z}_2\hat{\boldsymbol{a}}$, $\boldsymbol{Q}_{\hat{z}_1} = \boldsymbol{Z}_1\boldsymbol{Q}_{\hat{\mathrm{a}}}\boldsymbol{Z}_1{}^{\mathrm{T}}$, $\boldsymbol{Q}_{\hat{z}_2} = \boldsymbol{Z}_2\boldsymbol{Q}_{\hat{a}}\boldsymbol{Z}_2{}^{\mathrm{T}}$, $\boldsymbol{Q}_{\hat{z}_1\hat{z}_2} = \boldsymbol{Q}_{\hat{z}_2\hat{z}_1}^{\mathrm{T}} = \boldsymbol{Z}_1\boldsymbol{Q}_{\hat{a}}\boldsymbol{Z}_2{}^{\mathrm{T}}$, and $\boldsymbol{Q}_{\hat{z}_{2/1}} = \boldsymbol{Q}_{\hat{z}_2} - \boldsymbol{Q}_{\hat{z}_2\hat{z}_1}\boldsymbol{Q}_{\hat{z}_1}^{-1}\boldsymbol{Q}_{\hat{z}_1\hat{z}_2}$. In the PAR mode, only ambiguity subset $\hat{z}_1$ is fixed as integer solution $\check{z}_1$ by LAMBDA.

2.2. R-ratio-test-based ambiguity validation

The ambiguity validation that determines whether to accept the integer solution fixed in Section 2.1 is a non-trivial procedure for achieving high-precision positioning. The ratio test with an empirical threshold has been widely used for ambiguity validation. The most commonly used test is the R-ratio test, which can be defined as follows (Verhagen and Teunissen, 2006, 2013):

$$\frac{(\hat{\boldsymbol{a}}-\check{\boldsymbol{a}}_2)^{\mathrm{T}}\boldsymbol{Q}_{\hat{a}}^{-1}(\hat{\boldsymbol{a}}-\check{\boldsymbol{a}}_2)}{(\hat{\boldsymbol{a}}-\check{\boldsymbol{a}}_1)^{\mathrm{T}}\boldsymbol{Q}_{\hat{a}}^{-1}(\hat{\boldsymbol{a}}-\check{\boldsymbol{a}}_1)} = \frac{\boldsymbol{R}_2}{\boldsymbol{R}_1} \geq \mu \tag{5}$$

where μ is the tolerance value and R_i is the quadratic form of the ambiguity residuals of the best ($i=1$) and second-best ($i=2$) integer solutions, i.e., $\check{\boldsymbol{a}}_1$ and $\check{\boldsymbol{a}}_2$, respectively. Note that $\check{\boldsymbol{a}}_1$ can be accepted only when the ratio in Equation (5) is sufficiently large.

3. ADOP and two-dimensional convex hull theories

3.1. Single-epoch ADOP

The ADOP, first introduced by Teunissen (1997), is as an easy-to-compute scalar diagnostic for measuring the intrinsic model strength for successful ambiguity resolution. It can be defined as follows:

$$\mathrm{ADOP} = |\boldsymbol{Q}_{\hat{a}}|^{1/2n} \tag{6}$$

The ADOP for the geometry-based single-epoch single-baseline mode is given as follows (Odijk and Teunissen, 2008):

$$\mathrm{ADOP} \approx \frac{\sqrt{2}|\bar{\sigma}_\phi|}{\bar{\lambda}} \cdot \left[\frac{\sum_{s=1}^{m} w_s}{\prod_{s=1}^{m} w_s}\right]^{1/2n} \cdot \left[\frac{\bar{\sigma}_p}{\bar{\sigma}_\emptyset}\right]^{3/n} = f_1 \cdot f_2 \cdot f_3 \tag{7}$$

https://doi.org/10.1017/S0373463322000017 Published online by Cambridge University Press

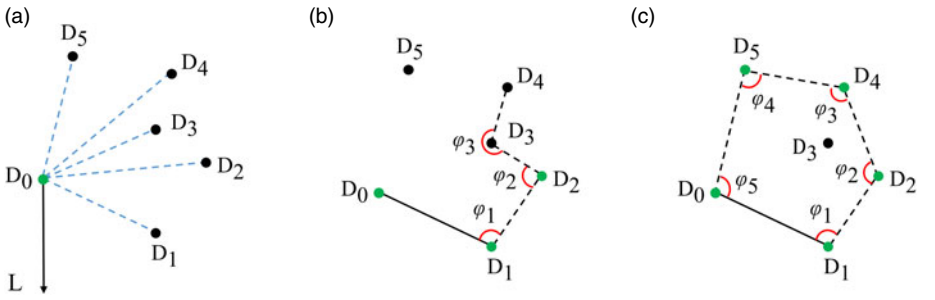

Figure 1. *Graham's scan algorithm for a convex hull.*

where $|\cdot|$ denotes the determinant, $\bar{\lambda} = \prod_{i=1}^{j} \lambda_i^{1/j}$, $\bar{\sigma}_\phi = \left(\left(\sigma_{\phi_1}^2 + \cdots + \sigma_{\phi_j}^2\right)\Big/ j\right)$, $\bar{\sigma}_p = \left(\left(\sigma_{p_1}^2 + \cdots + \sigma_{p_j}^2\right)\Big/ j\right)$, where j is the number of frequencies, and $w = (\sin\theta)^2$, where θ denotes the elevation angle. The ADOP also provides a good approximation to the integer least-squares success rate $P_{s,ILS}$ of the ambiguity resolution (Verhagen, 2003; Odijk and Teunissen, 2008):

$$P_{s,IB} \le P_{s,ILS} \approx P_{s,ADOP} = \left[2\Phi\left(\frac{1}{2ADOP}\right) - 1\right]^n \tag{8}$$

where $P_{s,ADOP}$ represents the ADOP-based success rate. Note that $P_{s,ADOP}$ and $P_{s,ILS}$ increase as ADOP decreases; the more ambiguities are involved, the steeper the decrease will be (Odijk and Teunissen, 2008).

3.2. Two-dimensional convex hull

The smallest convex set containing the given finite point set $\boldsymbol{S} = \{d_1, \cdots, d_k\}$ in Euclidean plane R^2 is called a two-dimensional convex hull whose vertices, called extreme points, belong to $\mathbf{S}$. Graham's Scan algorithm (Figure 1) is a well-known algorithm that constructs a sequence $\mathbf{D} = \{D_1, \cdots, D_5\}$ for all points in a polar coordinate system with D_0 as a pole, D_0L as the starting direction, and counter-clockwise as the positive direction (An, 2007). If the interior angle φ_i composed of the three adjacent points is not greater than π, then D_i is an extreme point. In Figure 1, D_0, D_1, D_2, D_4, and D_5 are extreme points.

4. PAR based on ADOP- and convex-hull-based satellite selection

In this section, the feasibility of ADOP as a threshold of PAR is analysed. Then, a novel PAR, i.e., ACPAR, is proposed. ADOP is invariant for a class of admissible ambiguity transformations, which makes it possible for ADOP to serve as a threshold for determining the ambiguity subset before ambiguity decorrelation. Based on Equation (7), ADOP can be predicted precisely by observed satellites that have a definite relationship with double-difference ambiguities. Hence, the ambiguity subset can be determined by selecting the corresponding satellites.

4.1. Feasibility analysis of ADOP as a threshold factor

To analyse the feasibility of ADOP as a PAR threshold, the corresponding parameters in Equations (1) and (2) are set as follows: $\boldsymbol{p} = \left[\boldsymbol{p}_1^{\mathrm{T}}\ \boldsymbol{p}_2^{\mathrm{T}}\right]^{\mathrm{T}}$, $\boldsymbol{\phi} = \left[\boldsymbol{\phi}_1^{\mathrm{T}}\ \boldsymbol{\phi}_2^{\mathrm{T}}\right]^{\mathrm{T}}$, $\boldsymbol{B} = \left[\boldsymbol{B}_1^{\mathrm{T}}\ \boldsymbol{B}_2^{\mathrm{T}}\right]^{\mathrm{T}}$, $\boldsymbol{a} = \left[\boldsymbol{a}_1^{\mathrm{T}}\ \boldsymbol{a}_2^{\mathrm{T}}\right]^{\mathrm{T}}$, $\boldsymbol{B}_\lambda = \begin{bmatrix} \boldsymbol{B}_{1,\lambda} & 0 \\ 0 & \boldsymbol{B}_{2,\lambda} \end{bmatrix}$, $\boldsymbol{Q} = \begin{bmatrix} \boldsymbol{Q}_1 & \boldsymbol{Q}_{12} \\ \boldsymbol{Q}_{21} & \boldsymbol{Q}_2 \end{bmatrix}$, and $\boldsymbol{P} = \begin{bmatrix} \boldsymbol{Q}_1^{-1} + \boldsymbol{Q}_1^{-1}\boldsymbol{Q}_{12}\boldsymbol{P}_2\boldsymbol{Q}_{21}\boldsymbol{Q}_1^{-1} & -\boldsymbol{Q}_1^{-1}\boldsymbol{Q}_{12}\boldsymbol{P}_2 \\ -\boldsymbol{P}_2\boldsymbol{Q}_{21}\boldsymbol{Q}_1^{-1} & \boldsymbol{P}_2 \end{bmatrix}$, where $\boldsymbol{P}_2 =$

https://doi.org/10.1017/S0373463322000017 Published online by Cambridge University Press

$[\boldsymbol{Q}_2 - \boldsymbol{Q}_{21}\boldsymbol{Q}_1^{-1}\boldsymbol{Q}_{12}]^{-1}$. When the parameters with the subscript '1' determined by satellite selection are used for positioning, the float ambiguity vector $\hat{\boldsymbol{a}}_1$ and its variance-covariance matrix are labelled as $\hat{\boldsymbol{a}}_1^{\mathrm{S}}$ and $\boldsymbol{Q}_{\hat{a}_1}^{\mathrm{S}}$, respectively. They are marked as $\hat{\boldsymbol{a}}_1^{\mathrm{P}}$ and $\boldsymbol{Q}_{\hat{a}_1}^{\mathrm{P}}$ with all the parameters used. The relationship between $\boldsymbol{Q}_{\hat{a}_1}^{\mathrm{S}}$ and $\boldsymbol{Q}_{\hat{a}_1}^{\mathrm{P}}$ can be expressed as follows (Liu et al., 2021):

$$\boldsymbol{Q}_{\hat{a}_1}^{\mathrm{P}} = \boldsymbol{Q}_{\hat{a}_1}^{\mathrm{S}} - \boldsymbol{A}_1 \tag{9}$$

where $\boldsymbol{A}_1 = \boldsymbol{B}_{1,\lambda}^{-1}\boldsymbol{B}_1\boldsymbol{A}_2\boldsymbol{B}_1^{\mathrm{T}}\boldsymbol{B}_{1,\lambda}^{-1}$ is a positive semidefinite matrix, $\boldsymbol{A}_2 = \boldsymbol{Q}_{\hat{b}}\boldsymbol{A}_3^{\mathrm{T}}(\boldsymbol{P}_2^{-1} + \boldsymbol{A}_3\boldsymbol{Q}_{\hat{b}}\boldsymbol{A}_3^{\mathrm{T}})^{-1}\boldsymbol{A}_3\boldsymbol{Q}_{\hat{b}}$, and $\boldsymbol{A}_3 = \frac{1}{\sigma_p}(\boldsymbol{Q}_{21}\boldsymbol{Q}_1^{-1}\boldsymbol{B}_1 - \boldsymbol{B}_2)$. For positive definite matrices $\boldsymbol{Q}_{\hat{a}_1}^{\mathrm{S}}$ and $\boldsymbol{Q}_{\hat{a}_1}^{\mathrm{P}}$, Equation (10) holds on the basis of Weyl's theorem (Lancaster and Tismenetsky, 1985) and Equations (6), (8), and (9):

$$\begin{cases} \mathrm{ADOP}^{\mathrm{P}} < \mathrm{ADOP}^{\mathrm{S}} \\ \mathrm{P}_{\mathrm{s,ADOP}}^{\mathrm{S}} < \mathrm{P}_{\mathrm{s,ADOP}}^{\mathrm{P}} \approx \mathrm{P}_{\mathrm{s,ILS}}^{\mathrm{P}} \end{cases} \tag{10}$$

where $\mathrm{ADOP}^{\mathrm{P}}$ and $\mathrm{ADOP}^{\mathrm{S}}$ represent the ADOP values of $\hat{\boldsymbol{a}}_1^{\mathrm{P}}$ and $\hat{\boldsymbol{a}}_1^{\mathrm{S}}$, respectively, $\mathrm{P}_{\mathrm{s,ADOP}}^{\mathrm{P}}$ and $\mathrm{P}_{\mathrm{s,ADOP}}^{\mathrm{S}}$ denote their ADOP-based success rates, respectively, and $\mathrm{P}_{\mathrm{s,ILS}}^{\mathrm{P}}$ denotes the integer least-squares success rate of $\hat{\boldsymbol{a}}_1^{\mathrm{P}}$.

The relation $\mathrm{P}_{\mathrm{s,ADOP}}^{\mathrm{S}} < \mathrm{P}_{\mathrm{s,ADOP}}^{\mathrm{P}}$ indicates that it is feasible to use the ADOP as the PAR threshold to determine the ambiguity subset by selecting satellites. Equation (8) indicates that $\mathrm{P}_{\mathrm{s,ADOP}}$ can estimate $\mathrm{P}_{\mathrm{s,ILS}}$ more accurately than $\mathrm{P}_{\mathrm{s,IB}}$. Hence, from the analyses presented above, compared with the conservative $\mathrm{P}_{\mathrm{s,IB}}$, ADOP is more suitable as a threshold for selecting partial ambiguities.

4.2. ADOP- and convex-hull-based ambiguity selection method

Rapidly determining the optimal ambiguity subset is of the utmost importance for PAR to achieve instantaneous high-precision positioning. Based on the positioning dilution of precision theory (Phillips, 1984), the selected ambiguities should correspond to the low- and high-elevation-angle satellites evenly distributed around the receiver. Hence, fast ambiguity selection methods based on ADOP- and convex-hull-based satellite selection are proposed in Sections 4.2.1 and 4.2.2.

4.2.1. Ambiguity selection based on convex-hull-based satellite selection

Compared with other points, the polygon area formed by the extreme points of the convex hull is maximum. Hence, an ambiguity selection method based on convex-hull-based satellite selection is first proposed to select the required ambiguities corresponding to evenly distributed low-elevation-angle satellites. In this method, convex-hull-based satellite selection, including the equipartition rotation method based on the convex hull and the method of the minimum inscribed circle of a polygon with the largest radius, is proposed to rapidly select low-elevation-angle satellites.

For the convex-hull-based equipartition rotation method, all the visible satellites are projected onto the XY plane of the local Cartesian coordinates, as shown in Figure 2(a): the circle represents the cutoff elevation angle, 'O' represents the master station, and the points represent the observed satellites.

Let us suppose that $m_{\mathrm{L}} = 3$ points evenly distributed around point O need to be selected from $m' = 9$ extreme points. The detailed strategy is as follows. (a) The starting line O1, together with the equipartition lines 1 and 2 in Figure 2(b), divides the circle evenly into m_{L} parts; each part is evenly divided by the blue dotted lines, which makes the circle evenly divided into sectors $\tilde{\varphi}_1$, $\tilde{\varphi}_2$, and $\tilde{\varphi}_3$, with the red lines as their bisectors. (b) For each sector, the extreme point with the smallest angular distance from its angle bisector is selected, i.e., the points 1, 4, and 7 in sectors φ_1, φ_2, and φ_3 in Figure 2(b). (c) The red and blue lines are rotated clockwise with point O as the origin until the starting line coincides with line O2, as shown in Figure 2(c). Step (b) is repeated and the points 2, 5, and 9 are selected. Step (c) is repeated until all the extreme points have been executed and there are at most $m' = 9$ sets of extreme points selected finally.

https://doi.org/10.1017/S0373463322000017 Published online by Cambridge University Press

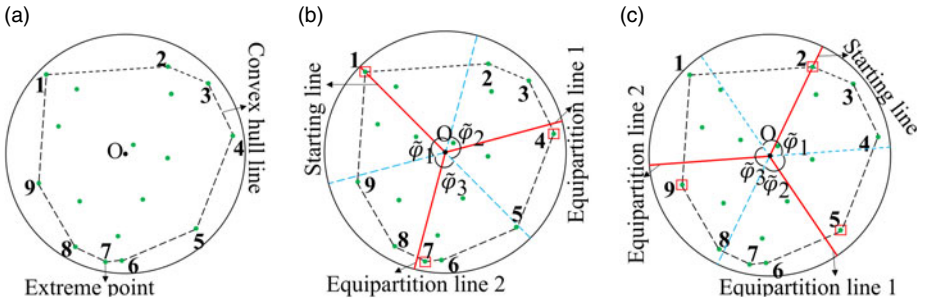

Figure 2. *Convex-hull-based equipartition rotation method.*

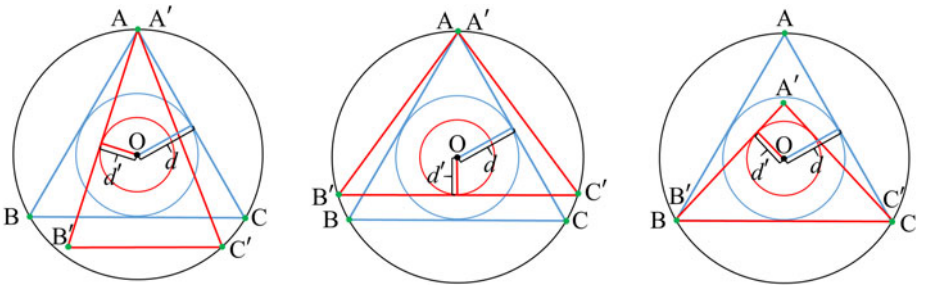

Figure 3. *Inscribed circle of a triangle with different radii.*

The optimal set that is most evenly distributed around point O needs to be determined from the selected point sets. Hence, the method of the largest-radius-based minimum inscribed circle of a polygon is proposed, in which the minimum inscribed circle of the polygon is the circle with point O as the centre and the shortest distance from point O to each side of the polygon as the radius.

In Figure 3, the blue circle with radius d and the red circle with radius d' are the minimum inscribed circles of ΔABC and ΔA′B′C′, respectively, where ΔABC is an equilateral triangle. The points of ΔABC are more evenly distributed around point O than those of ΔA′B′C′, and both the area and the radius of the blue circle of ΔABC are larger than those of ΔA′B′C′. Hence, it can be concluded that the more even the distribution of the points around point O, the larger is the radius of the minimum inscribed circle. The set of extreme points whose minimum inscribed circle has the largest radius is selected as the optimal point set. Hence, by the convex-hull-based satellite selection, the ambiguities corresponding to m_{L} low-elevation-angle satellites are selected first.

4.2.2. Ambiguity selection method based on ADOP-based satellite selection

The given ADOP ($\mathrm{ADOP}^{\mathrm{G}}$) can be achieved with the minimum number of high-elevation-angle satellites (Liu et al., 2019). Therefore, to realise fast positioning with a high success rate, an ambiguity selection method based on ADOP-based satellite selection is proposed to select the remaining ambiguities corresponding to high-elevation-angle satellites in the optimal subset based on $\mathrm{ADOP}^{\mathrm{G}}$.

To facilitate the analysis, the equation $\ln(\mathrm{ADOP}/f_1) = \alpha(\beta + \xi)$ is used, where $\alpha = \frac{1}{n}$, $\beta = \frac{1}{2}\ln\left(\sum_{s=1}^{m} w_s / \prod_{s=1}^{m} w_s\right)$, and $\xi = \ln(\bar{\sigma}_p/\bar{\sigma}_\emptyset)^3$, and $\ln(*)$ is the e-based logarithmic function. Further, β is selected as the threshold because only β is a variable for $\mathrm{ADOP}^{\mathrm{G}}$ with a known number of satellites for the determined system. From Equation (7), the theoretical $\tilde{\beta}$ and actual calculated $\bar{\beta}$ can be

https://doi.org/10.1017/S0373463322000017 Published online by Cambridge University Press

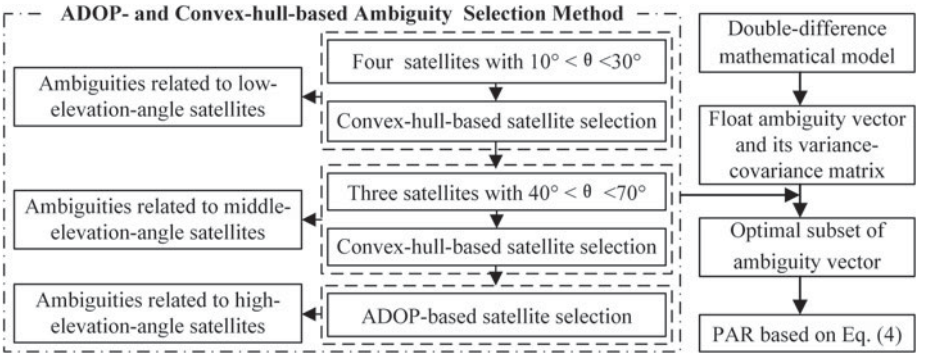

Figure 4. *Flowchart of ACPAR.*

written as follows:

$$\begin{cases} \tilde{\beta} = \dfrac{\ln(\mathrm{ADOP}/f_1)}{\alpha} - \xi \\ \bar{\beta} = \ln\left(\dfrac{\sum_{i=1}^{m_\mathrm{L}} w_i^\mathrm{L} + \sum_{s=1}^{m_\mathrm{H}} w_s^\mathrm{H}}{\prod_{i=1}^{m_\mathrm{L}} w_i^\mathrm{L} \cdot \prod_{s=1}^{m_\mathrm{H}} w_s^\mathrm{H}}\right)^{1/2} \end{cases} \tag{11}$$

where m_H is the number of selected high-elevation-angle satellites and $n = m_\mathrm{H} + m_\mathrm{L} - t$, where t denotes the number of reference satellites. When $\bar{\beta}$ is smaller than $\tilde{\beta}$, $\mathrm{ADOP}^\mathrm{P} < \mathrm{ADOP}^\mathrm{S} < \mathrm{ADOP}^\mathrm{G}$ and $\mathrm{P}^\mathrm{G}_{\mathrm{s,ADOP}} < \mathrm{P}^\mathrm{S}_{\mathrm{s,ADOP}} < \mathrm{P}^\mathrm{P}_{\mathrm{s,ADOP}}$ hold on the basis of Equation (10), where $\mathrm{P}^\mathrm{G}_{\mathrm{s,ADOP}}$ is the ADOP-based success rate calculated on the basis of ADOP^G.

The specific steps of the proposed method are as follows. First, $m_\mathrm{H} \geq t$ satellites with the highest elevation angles are selected from the remaining visible satellites. For ADOP^G, if $\bar{\beta}_1$ of the selected $m_\mathrm{L} + m_\mathrm{H}$ satellites calculated by Equation (11) is smaller than $\tilde{\beta}$, then the ambiguities corresponding to the selected satellites are the optimal subset. Otherwise, the highest-elevation-angle satellite in the remaining satellites is continuously selected and $\bar{\beta}_2$ of all the selected satellites is calculated. The above-mentioned process is repeated until $\bar{\beta}_\mathrm{i}$ of the selected satellites is smaller than the corresponding $\tilde{\beta}$. The ambiguity subset corresponding to the selected satellites is the optimal subset, which can be fixed by LAMBDA.

The method described in Section 4.2 is called ACPAR, and its flowchart is shown in Figure 4. The convex hull algorithm becomes more time-consuming as the number of satellites increases. To achieve fast positioning with more evenly distributed satellites, an elevation-angle-based layered processing strategy is proposed, as shown in the dotted box in Figure 4.

5. GPS/BDS/Galileo-based single-epoch positioning experiment

In this section, the GPS/BDS/Galileo systems are considered, as their signals are all based on the code-division multiple access technique. GLONASS was not considered, as the signals of most of its satellites are based on the frequency-division multiple access technique, which impedes straightforward integer resolution of the double-differenced ambiguities (Zaminpardaz et al., 2017). Single-epoch static and low-dynamic positioning experiments based on GPS/BDS/Galileo L1/B1/E1 and L2/B2/E5b were conducted in terms of the success rate, positioning accuracy, time consumption, and R-ratio test to validate the performance of ACPAR. The models for comparison include the ADOP- and convex-hull-based satellite selection (ACSS) described in the three dotted boxes in Figure 4, the classical PAR (CPAR), and L-multi-GNSS with a cutoff elevation angle of 10°. For CPAR, the float ambiguities with the highest accuracy were selected until $\mathrm{P}_{\mathrm{s,IB}}$ of the selected ambiguities was larger than the given threshold $\mathrm{P}^\circ_{\mathrm{s,IB}}$ and then fixed by LAMBDA. The above-mentioned data-processing algorithms were written in MATLAB R2016b based on goGPS (goGPS-project, 2021). The computer used for data

https://doi.org/10.1017/S0373463322000017 Published online by Cambridge University Press

Table 1. *Settings of different models.*

Frequency	Model	$ADOP^G$	$P^{\circ}_{s,IB}$	Labelled name
L1/B1/E1	ACSS	0·120/0·155	/	ACSS1-SF1/ACSS2-SF1
	ACPAR	0·135/0·155	/	ACPAR1-SF1/ACPAR2-SF1
L2/B2/E5b	ACSS	0·092/0·124	/	ACSS1-SF2/ACSS2-SF2
	ACPAR	0·105/0·124	/	ACPAR1-SF2/ACPAR2-SF2
L1/2/B1/2/E1/5b	ACPAR	0·155	/	ACPAR-DF1
		0·124	/	ACPAR-DF2
	CPAR	/	99·720%	CPAR-DF1
		/	99·976%	CPAR-DF2

processing was a Dell desktop with an Intel Core i7-7700 CPU (3·60 GHz) and 8·00 GB RAM. The baseline vector errors were obtained by subtracting the corresponding true values from the calculated baseline vectors. The empirical success rate $P_{s,E}$ was calculated as follows (Odolinski and Teunissen, 2016):

$$P_{s,E} = \frac{\text{Number of successful epochs}}{\text{Number of total epochs}} \tag{12}$$

where the successful epoch satisfied the following conditions: (i) the fixed ambiguities were the same as the reference ones that were determined by the multiple-frequency multi-GNSS with master and rover stations of known coordinates; (ii) the baseline vector deviations were all within certain ranges in the directions of East (E), North (N), and Up (U), the values of which were 10, 10, and 30 cm, respectively.

In this study, one pivot satellite between overlapping frequencies was used for double-difference observations. Hence, the L1/E1 parameters were labelled with the superscript 'GE' and they were labelled as 'BE' for B2/E5b. At B1/L1/E1, the average phase- and code-standard deviations were $\sigma_\emptyset{}^{GE+B} = 3 \cdot 033$ mm and $\sigma_p{}^{GE+B} = 31 \cdot 0$ cm, respectively, and the parameters were $f_1{}^{GE+B} \approx 0{\cdot}02247$, $f_3{}^{GE+B} \approx (102 \cdot 21)^{3/n}$, and $\xi^{GE+B} \approx 13{\cdot}88$. At B2/L2/E5b, they were $\sigma_\emptyset{}^{G+BE} = 3{\cdot}237$ mm, $\sigma_p{}^{G+BE} = 25 \cdot 667$ cm, $f_1{}^{G+BE} \approx 0 \cdot 01854$, $f_3{}^{G+BE} \approx (79 \cdot 29)^{3/n}$, and $\xi^{G+BE} \approx 13 \cdot 12$. The above-mentioned results were estimated using the method proposed by Odolinski et al. (2013); the data used were independent of those in the following sections.

5.1. GPS/BDS/Galileo-based static positioning

The 24 h and 5 km baseline data with a sampling interval of 1 s and 86,400 epochs from the Hong Kong base station were used in this section. The GPS/BDS/Galileo-based model settings are summarised in Table 1.

CPAR-DF*i* with given $P^{\circ}_{s,IB}$ can obtain the same average $P_{s,IB}$ as ACPAR-DF*i* ($i = 1, 2$). The $ADOP^G$ values of ACSS1-SF*i*, ACPAR1-SF*i*, and ACPAR-DF*i* are the maximum values for which the corresponding models can achieve $P_{s,E} = 100 \cdot 0\%$. For ACPAR-DF*i* and CPAR-DF*i*, only the ambiguities corresponding to the *i*th frequency were selected as the ambiguity subset. In addition, the L1/B1/E1-, L2/B2/E5b-, and L1/2/B1/2/E1/5b-based L-multi-GNSS were labelled as L-SF1, L-SF2, and L-DF, respectively. The number of observations of L-DF was twice that of L-SF*i* ($i = 1, 2$). Note that the satellites used for positioning selected by ACSS and ACPAR were the same, with the same $ADOP^G$, based on Figure 4.

5.1.1. GPS/BDS/Galileo-based positioning performance

The results of the different models are presented in Table 2 and Figures 5–8. The values before and after '/' in Table 2 denote the improvements in time consumption of the corresponding model relative

https://doi.org/10.1017/S0373463322000017 Published online by Cambridge University Press

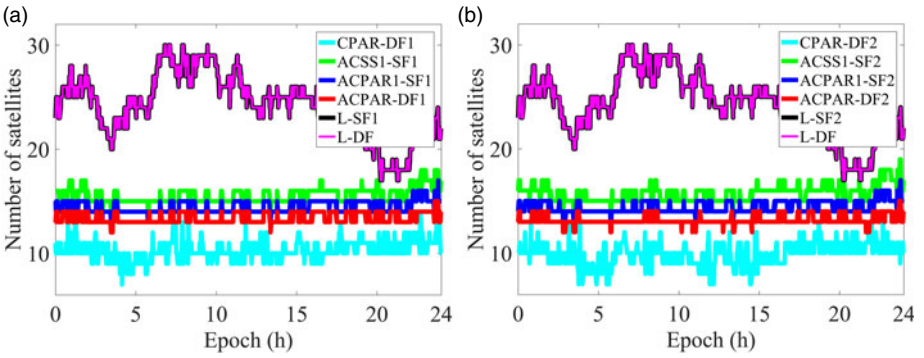

Figure 5. *Number of satellites of different models based on (a) L1/B1/E1 and (b) L2/B2/E5b.*

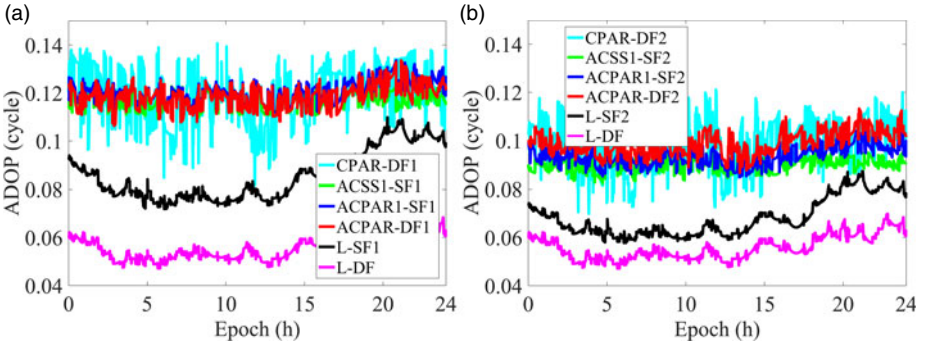

Figure 6. *ADOP of different models based on (a) L1/B1/E1 and (b) L2/B2/E5b.*

to L-SF*i* and L-DF, respectively. The average time consumption is defined by the total time divided by the total epochs, where the numerator is the period from the time at which the observation data were obtained to the time at which all the integer solutions of *b* were obtained. It should be emphasised that the positioning accuracy in the following tables is three-dimensional accuracy.

As shown in Table 2 and Figures 5 and 6, to achieve $P_{s,E} = 100 \cdot 0\%$, both the $ADOP^G$ values and the numbers of required satellites of ACSS1-SF*i*, ACPAR1-SF*i*, and ACPAR-DF*i* ($i = 1,\ 2$) decreased, whereas the ADOP values of ACPAR1-SF*i* and ACPAR-DF*i* were slightly larger than that of ACSS1-SF*i*. Hence, compared with ACSS, ACPAR could achieve $P_{s,E} = 100 \cdot 0\%$ with larger $ADOP^G$ and fewer satellites, although its ADOP was slightly larger. The above-mentioned phenomenon becomes more obvious with more observations. Based on Figure 6, the ADOP fluctuation of CPAR was larger than that of ACPAR, while the large ADOP values at some epochs denote a low success rate. Hence, the $P_{s,E}$ of CPAR-DF*i* was slightly smaller than that of ACPAR-DF*i*, although both its average $P_{s,IB}$ and ADOP were the same as those of ACPAR-DF*i*. This indicates that the ambiguity vectors fixed by CPAR were incorrect at some epochs albeit with large $\overset{\circ}{P}_{s,IB}$. Therefore, it can be concluded that ADOP is more suitable than $P_{s,IB}$ as a threshold for selecting the ambiguity subset.

According to Table 2, L-SF*i* and L-DF were most time-consuming owing to a large number of visible satellites. ACPAR, similarly to ACSS, could improve the computational efficiency of L-multi-GNSS considerably. The ACPAR1-SF*i* could improve the efficiency of L-SF*i*/L-DF by more than 54·9%/80·4% by selecting 14·4 out of 24·4 satellites. The corresponding improvement caused by ACPAR-DF*i* with 13·2 selected satellites was greater than 42·0%/75·8%, but it was smaller than that of ACPAR1-SF*i* owing to the large number of float parameters required to be calculated. However, the above-mentioned improvements were all larger than those of CPAR, although the number of satellites of CPAR was minimum; one reason was the similarity to ACPAR-DF*i*, while the other was the ambiguity decorrelation.

https://doi.org/10.1017/S0373463322000017 Published online by Cambridge University Press

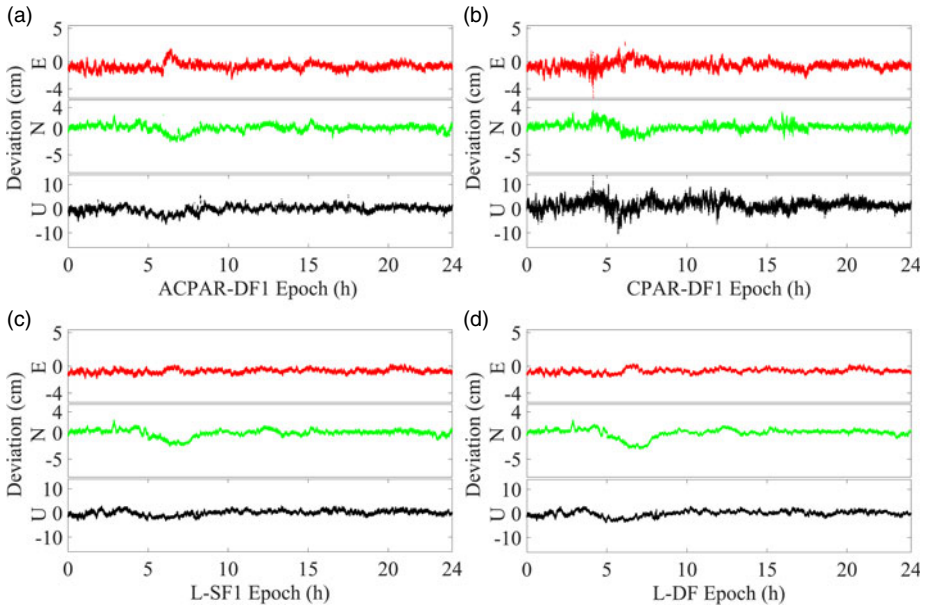

Figure 7. *ENU deviations of (a) ACPAR-DF1, (b) CPAR-DF1, and (c) L-SF1, (d) L-DF.*

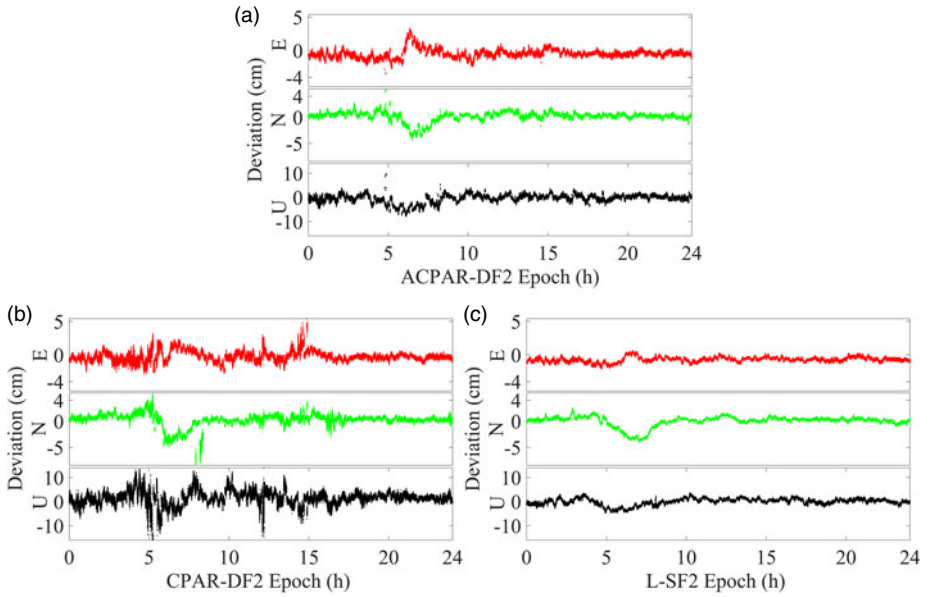

Figure 8. *ENU deviations of (a) ACPAR-DF2, (b) CPAR-DF2, and (c) L-SF2.*

According to Table 2, ACSS1-SF*i*, ACPAR1-SF*i*, and ACPAR-DF*i* had similar positioning accuracies close to L-SF*i* and L-DF with a maximum difference of 0·3 cm. Owing to the selected ambiguities corresponding only to the high-elevation-angle satellites, the positioning accuracy of CPAR-DF*i* was lower than that of ACPAR-DF*i* with a maximum difference of 1·1 cm. Based on the positioning accuracy results, Figures 7 and 8 show only the baseline vector errors of ACPAR-DF*i*, CPAR-DF*i*, L-SF*i*, and L-DF. The same trend of the positioning accuracy can be observed for the baseline vector accuracy according to Figures 7 and 8. Specifically, the baseline vector deviations in the E, N, and U (ENU)

https://doi.org/10.1017/S0373463322000017 Published online by Cambridge University Press

Table 2. *Positioning results of different models.*

Model	Number of satellites	ADOP	$P_{s,E}$(%)	Positioning accuracy (cm)	Average time consumption (ms)	Improvement (%)
ACSS1-SF1	15·6	0·117	100·00	1·3	16·8	53·46/79·18
ACPAR1-SF1	14·5	0·120	100·00	1·3	15·8	56·23/80·42
ACPAR-DF1	13·4	0·119	100·00	1·3	19·5	45·98/75·84
CPAR-DF1	10·3	0·119	99·99	2·2	23·7	34·35/70·63
ACSS1-SF2	15·8	0·090	100·00	1·5	15·9	51·23/80·30
ACPAR1-SF2	14·4	0·093	100·00	1·6	14·7	54·91/81·78
ACPAR-DF2	13·2	0·099	100·00	1·6	18·9	42·02/76·58
CPAR-DF2	9·9	0·099	99·97	2·7	24·9	23·62/69·14
L-SF1	24·4	0·085	100·00	1·2	36·1	/
L-SF2	24·4	0·068	100·00	1·4	32·6	/
L-DF	24·4	0·557	100·00	1·3	80·7	/

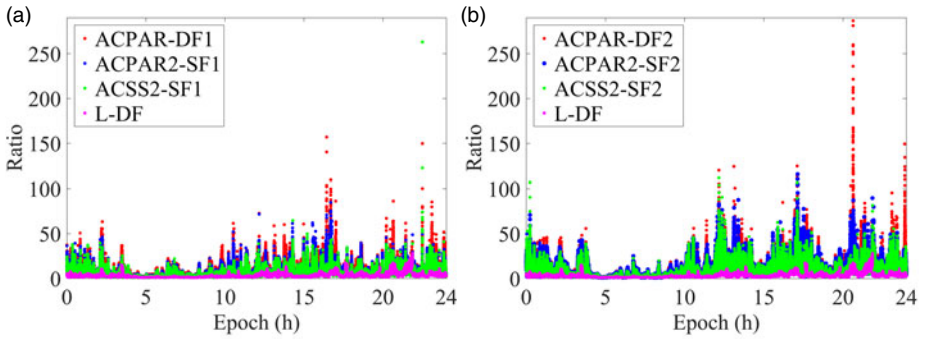

Figure 9. *Ratio values of different models based on (a) L1/B1/E1 and (b) L2/B2/E5b.*

directions of ACPAR-DF*i* were slightly larger than those of L-SF*i* and L-DF but smaller than those of CPAR-DF*i*.

In summary, for single-epoch positioning, compared with L-multi-GNSS, ACSS, and CPAR, ACPAR could simultaneously achieve high positioning accuracy, success rate, and computational efficiency, which also implies that ADOP is more suitable than $P_{s,IB}$ as a PAR threshold.

5.1.2. GPS/BDS/Galileo-based R-ratio test

In this section, μ is set to 1·5, 2·0, 2·5, and 3·0 (Verhagen and Teunissen, 2013). The results of ACSS2-SF*i*, ACPAR2-SF*i*, ACPAR-DF*i*, and L-DF (i = 1, 2) are presented in Table 3 and Figure 9.

Here, the acceptance rate $P_{a,R}$ is defined as the number of accepted epochs divided by 86,400, where an accepted epoch satisfies Equation (5). The successfully fixed rate $P_{sf,R}$ is defined as the ratio of the number of successfully fixed epochs satisfying Equation (5) to the number of accepted epochs, where the epochs in the numerator should meet conditions (i) and (ii) given after Equation (12). The false alarm rate $P_{fa,R}$ is defined as the ratio of the number of false alarm epochs to the number of successfully fixed epochs, where the number of false alarm epochs is equal to the number of successfully fixed epochs minus the number of accepted epochs. In this section, the success rate refers to the R-ratio-test-based success rate $P_{s,R}$ equal to $P_{sf,R} \cdot P_{a,R}$.

https://doi.org/10.1017/S0373463322000017 Published online by Cambridge University Press

Table 3. *R-ratio test results of different models.*

Model	Average ratio	$P_{a,R}$ (%)$P_{sf,R}/P_{fa,R}$ (%)			
		$\mu \geq 1 \cdot 5$	$\mu \geq 2 \cdot 0$	$\mu \geq 2 \cdot 5$	$\mu \geq 3 \cdot 0$
L-DF	3·15	84·79	66·12	50·64	38·94
		100·0/15·21	100·0/33·88	100·0/49·36	100·0/61·06
ACSS2-SF1	5·75	95·65	88·67	81·84	75·01
		99·99/4·02	100·0/11·00	100·0/17·86	100·0/24·71
ACPAR2-SF1	7·01	97·47	92·59	87·00	81·36
		100·0/2·44	100·0/7·33	100·0/12·93	100·0/18·57
ACPAR-DF1	8·29	98·40	94·88	90·60	86·03
		100·0/1·60	100·0/5·12	100·0/9·40	100·0/13·96
ACSS2-SF2	8·78	95·28	90·83	86·83	82·61
		99·96/3·69	99·99/8·19	100·0/12·24	100·0/16·50
ACPAR2-SF2	10·19	96·65	93·07	89·33	86·20
		100·0/3·26	100·0/6·84	100·0/10·59	100·0/13·72
ACPAR-DF2	11·35	97·47	93·92	90·83	87·68
		100·0/2·53	100·0/6·08	100·0/9·17	100·0/12·32

The results presented in Table 3 indicate that with a certain μ, $P_{a,R}$ of L-DF, ACSS2-SF*i*, ACPAR2-SF*i*, and ACPAR-DF*i* increased, which is consistent with the ratio values in Table 3 and Figure 9. When $i = 1$, for $P_{a,R}$, the maximum difference between ACSS2 and L-DF was around 36·1%, that between ACSS2 and ACPAR2 was around 6·4%, and that between ACSS2 and ACPAR-DF1 was around 11·0%. For $i = 2$, they were 43·7%, 3·6%, and 5·1%, respectively. Hence, both ACSS and ACPAR could improve $P_{a,R}$ of L-DF, while ACPAR could further improve $P_{a,R}$ of ACSS. Hence, the improvement caused by ACPAR increases with more satellite observations and $P_{a,R}$ of ACPAR could be up to 98·4%. Based on $P_{sf,R}$ equal or close to 100·0% and the relation of $P_{s,R} = P_{a,R} \cdot P_{sf,R}$, the same results and conclusion as those of $P_{a,R}$ could be obtained for $P_{s,R}$.

However, $P_{fa,R}$ showed opposite behavior: both ACSS and ACPAR could reduce $P_{fa,R}$ of L-DF, while ACPAR could further reduce $P_{fa,R}$ of ACSS. With $i = 1$, ACSS2 could reduce $P_{fa,R}$ of L-DF by up to 36·4%, while ACPAR2-SF1 and ACPAR-DF1 could reduce $P_{fa,R}$ of ACSS2 by up to 6·1% and 10·8%, respectively. For $i = 2$, they were 44·6%, 2·8%, and 4·2%, respectively. Further, $P_{fa,R}$ of ACPAR could reach 1·6%.

Ambiguity validation falls under carrier-phase-based integrity monitoring (Feng et al., 2009). Hence, in terms of the R-ratio-test-based ambiguity validation of single-epoch positioning, ACPAR could improve the reliabilities of the carrier-phase-based integrity monitoring of L-DF and ACSS: both ACPAR and ACSS could improve the ratio, $P_{a,R}$, and $P_{s,R}$ of L-DF, and reduce its $P_{fa,R}$, whereas the ACPAR could further improve the corresponding results of ACSS; these results become more obvious with more observations. The accuracy of low-elevation-angle satellite observations is easily and severely affected by ionospheric, tropospheric, and multipath errors, which will degrade the precision of the corresponding float ambiguities and affect the validation reliability of the entire ambiguity vector. Hence, the above-mentioned results of L-DF might be due to its large number of low-elevation-angle satellites.

5.2. L2/B2/E5b-based low-dynamic positioning

In this section, 1·5 h low-dynamic data with a sampling interval of 1 s, 5,218 epochs, and average speed of 30 km/h were collected using Trimble R10 from Xuzhou, China. As shown in Figure 10, one receiver was installed on the vehicle roof and another as the base station was placed on top of a building. The

https://doi.org/10.1017/S0373463322000017 Published online by Cambridge University Press

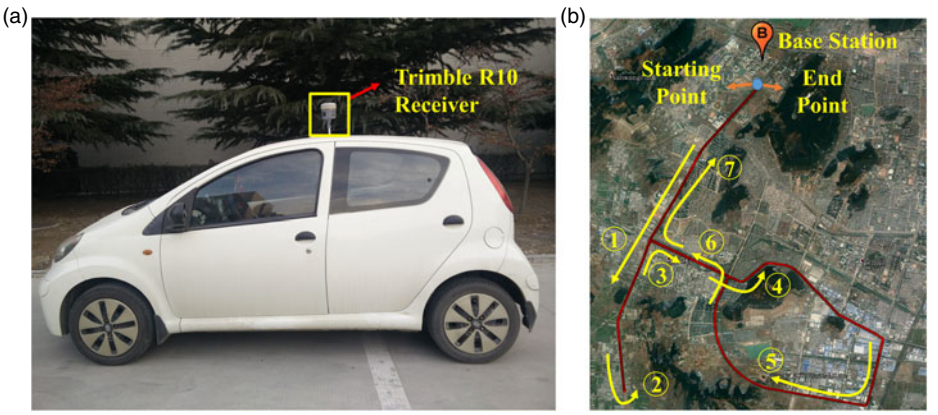

Figure 10. *(a) Experimental device and (b) movement trajectory.*

Table 4. *Positioning results of different models.*

Model	Number of satellites	ADOP	$P_{s,E}$ (%)	Positioning accuracy (cm)	Average time consumption (ms)	Improvement (%)
ACSS2-SF2	13·3	0·101	99·90	1·6	11·9	80·20
ACPAR-DF2	13·3	0·087	100·00	1·6	16·5	72·55
CPAR-DF2	9·8	0·095	99·88	4·0	20·2	66·39
L-DF	20·0	0·053	100·00	1·9	60·1	/

red line represents the movement trajectory with a maximum distance from the base station of around 8·0 km. The yellow directional lines and the numbers from small to large represent the driving direction and sequence of the vehicle, respectively. For urban canyon conditions, the experimental settings shown in Figure 4 were adjusted as follows: the step 'Ambiguities related to middle-elevation-angle satellites' was abandoned; θ in 'Ambiguities related to low-elevation-angle satellites' was set to $10^{\circ} \le \theta \le 50^{\circ}$. According to the results presented in the previous section, L2/B2/E5b-based positioning can achieve smaller ADOP with a similar number of satellites compared with L1/B1/E1. Hence, ACSS2-SF2, ACPAR-DF2, CPAR-DF2, and L-DF were used, for which $P^{\circ}_{s,IB}$ and $ADOP^{G}$ were set to 99·995% and 0·105, respectively.

5.2.1. L2/B2/E5b-based positioning performance

Table 4, together with Figures 11 and 12, presents the positioning accuracy, ADOP, $P_{s,E}$, time consumption, and corresponding improvement results of the different models.

As shown in Table 4, the $P_{s,E}$ values of both ACPAR-DF2 and L-DF were up to 100·00% larger than that of ACSS2-SF2, while the ADOP of ACPAR-DF2 was smaller than that of ACSS2-SF2, although the same satellites were used for positioning. Hence, compared with ACSS, ACPAR could achieve higher $P_{s,E}$ and smaller ADOP with the same satellites and $ADOP^{G}$. According to the ADOP and $P_{s,E}$ results shown in Table 4 and Figure 11, the similar relationship between CPAR-DF2 and ACPAR-DF2 compared with that described in Section 5.1.1 indicates that the conclusion drawn in the previous section is still valid.

Table 4 and Figures 11 and 12 show that the trends in the time consumption and positioning accuracy between ACSS2-SF2, ACPAR-DF2, CPAR-DF2, and L-DF are similar to those in Section 5.1.1. Hence, in the above-mentioned aspects, the same conclusions as those in the previous section can be obtained

https://doi.org/10.1017/S0373463322000017 Published online by Cambridge University Press

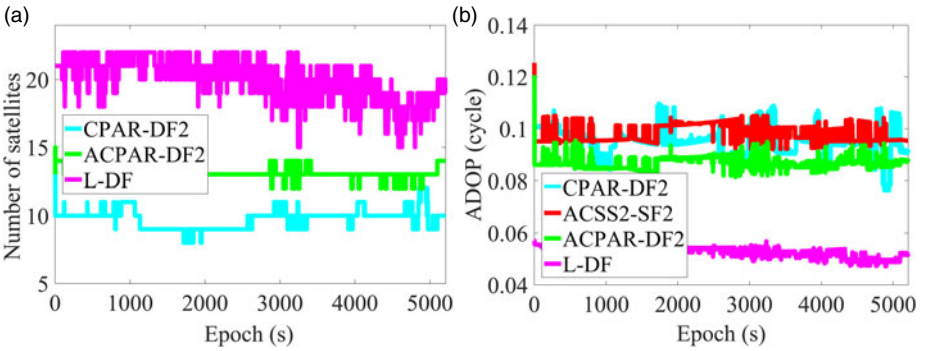

Figure 11. *(a) Number of satellites and (b) ADOP of different models.*

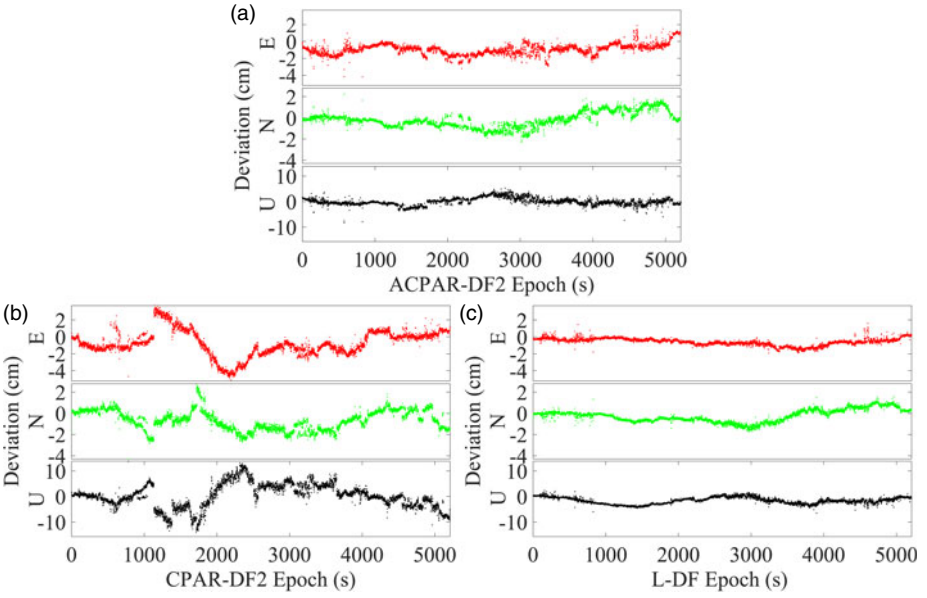

Figure 12. *ENU deviations of (a) ACPAR-DF2, (b) CPAR-DF2, and (c) L-DF.*

in this section. However, there were some discrepancies. By selecting 13·3, 13·3, and 9·8 out of 20·0 satellites, respectively, ACSS-SF2, ACPAR-DF2, and CPAR-DF2 could improve the efficiency of L-DF by more than 80·0%, 72·5%, and 66·0%, respectively. In terms of the positioning accuracy, similar to ACSS-SF2, the positioning accuracy of ACPAR-DF2 was up to 1·6 cm, which was higher than those of L-DF and CPAR-DF2 with differences of around 0·3 and 2·4 cm, respectively. The positioning accuracy of L-DF was lower than that of ACPAR-DF2, which may be due to the large number of low-elevation-angle satellites in L-DF. Compared with high-elevation-angle satellites, low-elevation-angle satellite signals are severely affected by ionospheric and tropospheric delay errors, and are vulnerable to multipath errors, which will adversely affect the positioning accuracy and ambiguity resolution success rate.

In summary, in terms of L2/B2/E5b-based low-dynamic single-epoch positioning, compared to L-multi-GNSS, ACSS, and CPAR, ACPAR could simultaneously achieve fast and high-precision positioning with a high success rate, which again proves that ADOP is more suitable than $P_{s,IB}$ as a PAR threshold.

https://doi.org/10.1017/S0373463322000017 Published online by Cambridge University Press

Table 5. *R-ratio test results of different models.*

Model	Average ratio	$P_{a,R}$ (%) $P_{sf,R}/P_{fa,R}$(%) $\mu \geq 1 \cdot 5$	$\mu \geq 2 \cdot 0$	$\mu \geq 2 \cdot 5$	$\mu \geq 3 \cdot 0$
L-DF	3·22	96·16 100·0/3·84	80·99 100·0/17·32	58·42 100·0/41·58	41·56 100·0/58·44
ACSS2-SF2	5·35	97·64 100·0/2·27	94·99 100·0/4·92	92·17 100·0/7·74	84·14 100·0/15·97
ACPAR-DF2	7·00	99·79 100·0/0·21	99·48 100·0/0·52	94·80 100·0/5·20	90·54 100·0/9·46

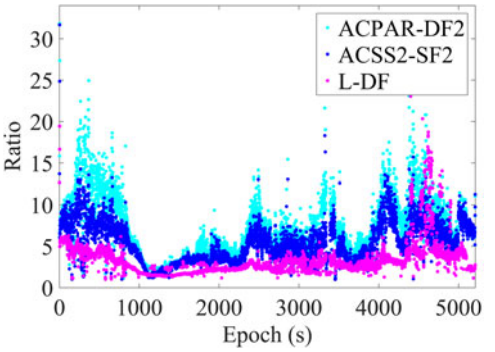

Figure 13. *Ratio values of different models.*

5.2.2. L2/B2/E5b-based R-ratio test

In this section, the same values were used for μ as those in Section 5.1.2; here, the success rate refers to $P_{s,R}$. The R-ratio test results of L-DF, ACSS2-SF2, and ACPAR-DF2 are presented in Table 5 and Figure 13.

Table 5 and Figure 13 show that in terms of the ratio, $P_{a,R}$, $P_{sf,R}$, and $P_{fa,R}$, the relationships between ACSS2-SF2, ACPAR-DF2, and L-DF are the same as those in Section 5.1.2. Hence, in terms of $P_{s,R}$ and the above-mentioned aspects, the same conclusions as those in Section 5.1.2 can be drawn in this section with some changes. The maximum difference of $P_{a,R}$ between ACSS-SF2 and L-DF was around 42.6% and that between ACSS-SF2 and ACPAR-DF2 was around 6·4%. For $P_{fa,R}$, the maximum differences between ACSS-SF2 and L-DF and between ACPAR-DF2 and ACSS-SF2 were around 42·5% and 6.5%, respectively. Further, $P_{a,R}$, $P_{s,R}$, and $P_{fa,R}$ of ACPAR could reach 99·79%, 99·79%, and 0·21%, respectively.

Therefore, in terms of R-ratio-test-based ambiguity validation of L2/B2/E5b-based low-dynamic single-epoch positioning, ACPAR has the same advantages as the statistic positioning experiments in Section 5.1.2.

6. Conclusion

Owing to the wide applications of fast positioning, GNSS-based single-epoch positioning has long been a research hotspot. Although multi-GNSS can improve the success rate, its large number of visible satellites make positioning time-consuming. PAR can improve the efficiency of multi-GNSS by selecting partial ambiguities. However, the present PAR cannot simultaneously achieve fast and high-precision positioning with a high success rate. To address this issue, this paper proposed a novel PAR, i.e., ACPAR.

https://doi.org/10.1017/S0373463322000017 Published online by Cambridge University Press

The feasibility of ADOP as the PAR threshold was analysed theoretically. Further, ambiguity selection based on ACSS was proposed to determine the optimal ambiguity subset by rapidly and adaptively selecting the corresponding satellites satisfying $ADOP^G$. The following conclusions can be drawn from the static and low-dynamic single-epoch positioning results of ACPAR, ACSS, the classical PAR, and L-multi-GNSS:

(a) ACPAR can achieve a higher success rate and more stable ADOP than the classical PAR with the same $P_{s,IB}$, which indicates that ADOP is more suitable than $P_{s,IB}$ as a threshold for determining the ambiguity subset; compared to ACSS, ACPAR can achieve a higher success rate and smaller ADOP with the same satellites and $ADOP^G$.
(b) Similar to ACSS, ACPAR can achieve high positioning accuracy close to that of L-multi-GNSS and higher than that of the classical PAR with maximum differences of 0·3 and 2·4 cm, respectively. ACPAR outperforms the classical PAR and it improves the efficiency of L-multi-GNSS considerably. The improvements caused by single (dual) frequency-based ACPAR are greater than 54·9%/80·4% (42·0%/75·8%) when 14·4 (13·2) out of 24·4 single/dual-frequency L-multi-GNSS satellites are selected.
(c) From the perspective of R-ratio-test-based ambiguity validation, ACPAR can improve the reliabilities of the carrier-phase-based integrity monitoring of L-multi-GNSS and ACSS: ACSS can improve $P_{a,R}$ and $P_{s,R}$ and reduce $P_{fa,R}$ of L-multi-GNSS by up to 43·7%, 43·7%, and 44·6%, respectively; ACPAR can further improve the corresponding results of ACSS by up to 11·0%, 11·0%, and 10·8%, respectively.

In the future, the large number of visible satellites in GPS, BDS, GLONASS, and Galileo will make positioning more time-consuming. By then, the advantages of ACPAR will be more obvious. Focus areas for further research include the mechanism of float ambiguity vector precision affecting the reliability of ambiguity validation and how to further improve the acceptance rate and reduce the false alarm rate of ACPAR.

Acknowledgments. The authors are very grateful for the comments and remarks of the reviewers who helped to improve the manuscript. This work was supported by the Fundamental Research Funds for the Central Universities (Grant No. 2019XKQYMS52).

References

An, P. (2007). A modification of Graham's algorithm for determining the convex hull of a finite planar set. *Annales Mathematicae et Informaticae*, **34**, 3–8.

BeiDou Navigation Satellite System. (2021). BDS Ephemeris 2021-082. Available at: http://en.beidou.gov.cn/SYSTEMS/Ephemeris/ [Accessed 23 March 2021].

Brack, A. (2017). Reliable GPS+BDS RTK positioning with partial ambiguity resolution. *GPS Solutions*, **21**, 1083–1092.

Brack, A. and Christoph, G. (2014). Generalized integer aperture estimation for partial GNSS ambiguity fixing. *Journal of Geodesy*, **88**, 479–490.

Deng, C., Tang, W., Liu, J. and Shi, C. (2014). Reliable single-epoch ambiguity resolution for short baselines using combined GPS/Beidou system. *GPS Solutions*, **18**, 375–386.

European GNSS Service Centre. (2021). Constellation Information. Available at: https://www.gsc-europa.eu/system-service-status/constellation-information [Accessed 23 March 2021].

Feng, S., Ochieng, W., Moore, T., Hill, C. and Hide, C. (2009). Carrier phase-based integrity monitoring for high-accuracy positioning. *GPS Solutions*, **13**, 13–22.

goGPS-project. (2021). goGPS_MATLAB. Available at: https://github.com/goGPS-Project/ [Accessed 23 March 2021].

GPS.GOV. (2021). Current and Future Satellite Generations. Available at: https://www.gps.gov/systems/gps/space/#generations [Accessed 23 March 2021].

Han, S. and Rizos, C. (1999). Single-epoch ambiguity resolution for real-time GPS attitude determination with the aid of one-dimensional optical fiber gyro. *GPS Solutions*, **3**, 5–12.

Lancaster, P. and Tismenetsky, M. (1985). *The Theory of Matrices with Applications*. San Diego: Academic Press.

Li, J., Yang, Y., Xu, J., He, H. and Gou, H. (2015). GNSS multi-carrier fast partial ambiguity resolution strategy tested with real BDS/GPS dual- and triple-frequency observations. *GPS Solutions*, **19**, 5–13.

Liu, X., Chen, G., Zhang, Q. and Zhang, S. (2017). Improved single-epoch single-frequency PAR LAMBDA algorithm with baseline constraints for the BeiDou navigation satellite system. *IET Radar, Sonar & Navigation*, **11**, 1549–1557.

Liu, X., Zhang, S., Zhang, Q., Ding, N. and Yang, W. (2019). A fast satellite selection algorithm with floating high cut-off elevation angle based on ADOP for instantaneous multi-GNSS single-frequency relative positioning. *Advances in Space Research*, **63**, 1234–1252.

Liu, X., Zhang, S., Zhang, Q., Zheng, N., Zhang, W. and Ding, N. (2021). Theoretical analysis of the multi-GNSS contribution to partial ambiguity estimation and R-ratio test-based ambiguity validation. *GPS Solutions*, **25**, 52.

Mowlam, A. (2004). Baseline Precision Results Using Triple Frequency Partial Ambiguity Sets. *Proceedings of the 17th International Technical Meeting of the Satellite Division of the Institute of Navigation (*ION GNSS *2004)*, Long Beach, CA.

Odijk, D. and Teunissen, P. (2008). ADOP in closed form for a hierarchy of multi-frequency single-baseline GNSS models. *Journal of Geodesy*, **82**, 473–492.

Odolinski, R. and Teunissen, P. (2016). Single-frequency, dual-GNSS versus dual-frequency, single-GNSS: A low-cost and high-grade receivers GPS-BDS RTK analysis. *Journal of Geodesy*, **90**, 1255–1278.

Odolinski, R., Teunissen, P. and Odijk, D. (2013). An Analysis of Combined COMPASS/BeiDou-2 and GPS Single- and Multiple-Frequency RTK Positioning. *Proceedings of the* ION *2013 Pacific* PNT *Meeting*, Honolulu, Hawaii.

Odolinski, R., Teunissen, P. and Odijk, D. (2015). Combined BDS, Galileo, QZSS and GPS single-frequency RTK. *GPS Solutions*, **19**, 151–163.

Parkins, A. (2011). Increasing GNSS RTK availability with a new single-epoch batch partial ambiguity resolution algorithm. *GPS Solutions*, **15**, 391–402.

Phillips, A. (1984). Geometrical determination of PDOP. *Navigation*, **31**, 329–337.

Takasu, T. and Yasuda, A. (2010). Kalman-filter-based integer ambiguity resolution strategy for long-baseline RTK with ionosphere and troposphere estimation. *Proceedings of the 23rd International Technical Meeting of the Satellite Division of the Institute of Navigation (*ION GNSS *2010)*, Portland, OR.

Teunissen, P. (1995). The least-squares ambiguity decorrelation adjustment: A method for fast GPS integer ambiguity estimation. *Journal of Geodesy*, **70**, 65–82.

Teunissen, P. (1997). A canonical theory for short GPS baselines. Part IV: Precision versus reliability. *Journal of Geodesy*, **71**, 513–525.

Teunissen, P., Joosten, P. and Tiberius, C. (1999). Geometry-free Ambiguity Success Rates in Case of Partial Fixing. *Proceedings of the 1999 National Technical Meeting of the Institute of Navigation*, San Diego, CA.

Teunissen, P., Odolinski, R. and Odijk, D. (2014). Instantaneous BeiDou + GPS RTK positioning with high cut-off elevation angles. *Journal of Geodesy*, **88**, 335–350.

Verhagen, S. (2003). On the approximation of the integer least-squares success rate: Which lower or upper bound to use? *Journal of Global Position Systems*, **2**, 117–124.

Verhagen, S. and Teunissen, P. (2006). New global navigation satellite system ambiguity resolution method compared to existing approaches. *Journal of Guidance, Control, and Dynamics*, **29**, 981–991.

Verhagen, S. and Teunissen, P. (2013). The ratio test for future GNSS ambiguity resolution. *GPS Solutions*, **17**, 535–548.

Verhagen, S., Teunissen, P., Marel, H. and Li, B. (2011). GNSS Ambiguity Resolution: Which Subset to Fix. *Proceedings of International Global Navigation Satellite Systems Society,* IGNSS *Symposium 2011*, Sydney, NSW, Australia.

Yang, Y., Li, J., Xu, J., Tang, J., Guo, H. and He, H. (2011). Contribution of the compass satellite navigation system to global PNT users. *Chinese Science Bulletin*, **56**, 2813–2819.

Yi, T., Li, H. and Gu, M. (2013). Experimental assessment of high-rate GPS receivers for deformation monitoring of bridge. *Measurement*, **46**, 420–432.

Zaminpardaz, S., Teunissen, P. and Nadarajah, N. (2017). GLONASS CDMA l3 ambiguity resolution and positioning. *GPS Solutions*, **21**, 535–549.

Cite this article: Liu X, Zhang S, Zhang Q, Zheng N, Zhang W, Ding N (2022). A novel partial ambiguity resolution based on ambiguity dilution of precision- and convex-hull-based satellite selection for instantaneous multiple global navigation satellite systems positioning. *The Journal of Navigation* **75**: 4, 832–848. https://doi.org/10.1017/S0373463322000017